Chemical Communications

COMMUNICATION

Supplementary information

Nonstoichiometry induced Broadband Tunable Photoluminescence of Monolayer WSe_2

Weitao Su[a*], Yongguang Li[a], Leifeng Chen[a], Dexuan Huo[a] ,Kaixin Song[b], Xiwei Huang[c], Haibo Shu[d,*]

[a]College of Materials and Environmental Engineering, Hangzhou Dianzi University, 310018, Hangzhou, China

[b] College of Electronics and Information, Hangzhou Dianzi University, 310018, Hangzhou, China

[c]Key Laboratory of RF Circuits and Systems (Hangzhou Dianzi University), Ministry of Education, Hangzhou ,310 018, China

[d] College of Optical and Electronic Technology, China Jiliang University 310018, Hangzhou, China

Email: suweitao@hdu.edu.cn; shu123hb@gmail.com

§S1 Growth of different monolayer WSe_2 samples

Four monolayer WSe_2 samples with different W/Se ratio were prepared either by VT (M1, M2 and M4, Fig.1a) or CVD growth(M3, Fig.1b) method. Cleaned SiO_2(thickness 300nm)/Si were used as substrates. In VT growth, high purity(99.5%) WSe_2 powder was used as the source material. In CVD growth, high purity of selenium(Se) and WO_3 powders were used as precursors for Se and W, respectively. Before increasing the temperature, the tube furnace was pumped to a vacuum < 1Pa. The furnace temperature was raised to 900℃ for M3 and 950℃ for other samples at a rate of 20℃/min. The vacuum was kept at 100Torr for M3 and 20Torr for the other samples. After growth finalized, the furnace was rapidly cooled down to room temperature under flowing carrier gas.

(1) In deposition of M1, the WSe_2 source material was placed downstream ~10cm away from the center of a quartz tube furnace. Water solutions of GQDs were spin-coated on substrates for growth of WSe_2 flakes. The substrates were placed downstream ~12cm away from the source. Ar_2/H_2(volume ratio=19/1) with flow rate of 15sccm was introduced as carrier gas . The growth time was 30 mins.

(2) In deposition of M2, the WSe_2 source material was placed downstream ~10cm away from the center of a quartz tube furnace. Substrates were placed downstream ~12cm away from the source. N_2 with flow rate of 17sccm was introduced as carrier gas. The growth time was 40min.

(3) In deposition of M3, the Se powder(300mg) was placed upstream ~4cm away from center of a quartz tube furnace. WO_3 powder(20mg) was placed downstream ~15cm away from center of a quartz tube furnace. Substrates were placed at the position of WO_3 powders and facing down. Ar_2/H_2(volume ratio=19/1) with flow rate of 15sccm was introduced as carrier gas . The growth time was 10min.

(4) In deposition of M4, the WSe_2 source material was placed downstream ~8cm away from the center of a quartz tube furnace. Substrates were placed downstream ~12cm away from the source. Ar_2/H_2(volume ratio=19/1) with flow rate of 15sccm was introduced as carrier gas. The growth time was 60min.

$$WSe_2 \xrightarrow[\text{sublimation}]{\text{Decomposition,}} W + 2Se \xrightarrow{\text{Growth}} W_xSe_y + (1-x)W + (2-y)Se \qquad \text{(S1)}$$

$$WSe_2 + 2H_2 \xrightarrow[\text{sublimation}]{\text{Decomposition,}} W + 2H_2Se \xrightarrow{\text{Growth}} WxSe_y + (1-x)W + (2-y)H_2Se + yH_2 \qquad \text{(S2)}$$

$$WO_3 + ySe + zH_2 \xrightarrow[\text{sublimation}]{\text{Reaction,}} W + yH_2Se + 3H_2O + (z-y-3)H_2 \xrightarrow{\text{Growth}} WSe_x + (y-x)H_2Se + 3H_2O + (z-y-3)H_2$$

(S3)

The length of constant temperature zone of our tube furnace is 20cm. In the deposition of M4, the source temperature is 950 °C. Sinc

temperature zone, their temperatures are 920-930 °C.

The vapor transport growth of WSe_2 sample M2 with N_2 as carrier gas can be depicted by eq.S1. In this case WSe_2 decomposits and sublimates at ~920°C. The vapor of W and Se transport for 12cm and grow into WSe_2 flakes at low temperature. However, due to low partial pressure of W high partial pressure of Se, a Se-rich WSe_2 monolayer is obtained.

In the deposition using Ar/H_2 as carrier gas, H_2Se is expected to be formed, which enhances the sublimation of WSe_2(possibly from eq.S2). This hydrogen-assisted sublimation are usually observed in the sublimation of most of selenides. In this case, sublimation is expected to be much easier, and the partial pressure of H_2Se is expected to be higher than that using pure N_2 as carrier gas[1]. The stoichiometry of the obtained WSe_2 films also strongly depends on the temperature of source and the sample-source distance. The source sublimation temperature in preparation of M1 is lower than that of M4. Tungsten has low partial pressure at lower temperature, but the pressure of selenide is still high owing to the formation of H_2Se. Moreover, the growth temperature of M1 is also much lower than M4, which causes even low content of tungsten at the growth area. Therefore, the as-prepared WSe_2 flake is expected to be selenium rich. While for M4, the sublimation temperature is high, while the growth temperature is also high, which causes larger content of tungsten.

The CVD growth of WSe_2 can be depicted as eq.S3. In this case extra large amount of Se was used . We tried pure Ar as carrier gas, whereas no WO_3 sublimation was observed. When we used Ar/H_2 as carrier gas, no sublimation was observed when the pressure was lower than 50 Torr. As a result, H_2-assited reaction of WO_3 into W is introduced as an important step. The intermediates, H_2Se and W then react into WSe_2[1] . As shown in Fig.1a, the substrate is placed faced down on the top of crucible. WSe_2 only grows at the edge of substrate. Only at the edge, the W/Se ratio is close the growth condition, while at the center, the W/Se ratio is too large and no WSe_2 flakes grow. Low growth temperature (900℃) also helps the growth of W-rich sample using CVD routine.

§S2 Characterization and calculation.

Optical images of WSe_2 samples were obtained using an optical microscope. Raman spectra of WSe_2 samples were measured using a Raman spectrometer(Invia, Renishaw) with excitation laser wavelength of 532nm with laser power ~0.05mW. PL mapping were conducted on a PL/Raman spectrometer(Xplora, Horiba) with excitation laser wavelength of 532 nm and laser power of 0.1mW. In PL mapping, 600 grooves/mm grating was used. Resonant Raman measurement excited by 532nm and 633nm lasers were recorded on a home-built Raman system consisted by a Nikon Ti inverted microscope and a Horiba iHR320 Raman spectrometer with a Sincerity CCD. All the Raman spectra were calibrated using silicon peak at 520cm^{-1}. Auger spectra were obtained on a nano Auger electron spectroscopy(Phi710, Ulvac-Phi) at acceleration voltage of 10kV.

All DFT calculations were performed using the projector augmented wave (PAW) method[2] as implemented in the Vienna *ab initio* Simulation Package (VASP)[3, 4]. The electronic exchange-correlation energy was treated by generalized-gradient approximation (GGA) of Perdew-Burke-Ernzerhof (PBE).[5] A kinetic cutoff energy of 400 eV was used for the plane-wave expansion set. The *k*-point sampling in the Brillouin zone was implemented by the Monkhorst-Pack scheme with the grids of 4×4×1 for the 5×5 WSe_2 supercells. For the geometry optimization, the convergence criteria of energy and forces acting on each atom were 10^{-3} eV and 10^{-2} eV/Å, respectively. To evaluate the stability of various defective structures, their formation energies have been calculated by the following equation

$$E_f = E_D - E_T + \Delta n_i \sum_i \mu_i \qquad \text{(S4)}$$

where E_D and E_T are total energies of monolayer WSe_2 with and without intrinsic defects, respectively. μ_i is the chemical potential of atomic species i (i = W and Se), and Δn_i is the difference of the number of W and Se atoms between perfect and defective structures. To maintain thermodynamic equilibrium (i.e., $\mu_{WSe2} = \mu_W + 2\mu_{Se}$), the allowable range of μ_{Se} is $\mu_{Se(bulk)} - \Delta H_f/2 < \mu_{Se} < \mu_{Se(bulk)}$, where the upper (lower) limit corresponds to Se-rich (Mo-rich) condition and ΔH_f is the heat of formation. Here ΔH_f is defined as $\Delta H_f = E_{WSe2} - E_W - 2E_{Se}$, where E_{WSe2}, E_W, and E_{Se} are the energies of WSe_2 monolayer, W and Se atoms in bulk, respectively. The computed ΔH_f is 1.70 eV.

§S3 Optical images and PL spectra of monolayer and few-layer WSe_2 samples

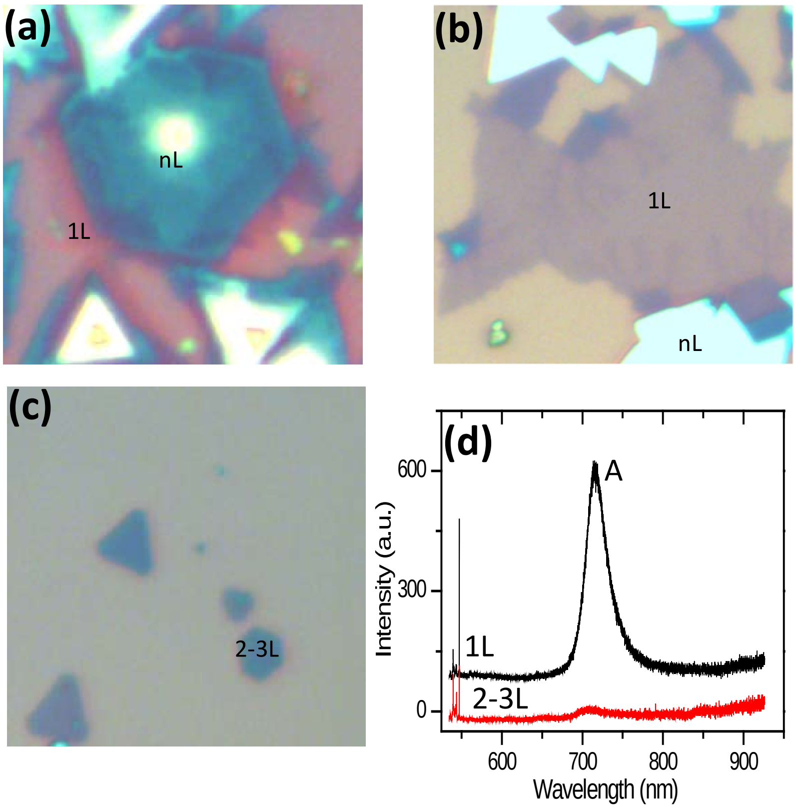

Fig. S1 Optical images of M2(a), M3(b) and few layers(c); (d) PL spectra of few-layers as comparison to monolayer.

§S4 AFM image analysis

An AFM topographic image, which corresponds to monolayer flakes of M4, is shown in Fig.S2a. Three line profiles along marked lines L1, L2 and L3 in Fig.S2a are plotted in Fig.S2c. The thickness of three flakes are calculated to be 0.72nm, 0.73nm and 0.9nm for L1, L2 and L3, respectively. These values give an average thickness as 0.78nm, which agrees well to the reported thickness of monolayer WSe_2 as 0.7nm[6]. An AFM image of M1 is shown in Fig.S2b, which corresponds well with the optical image in Fig. 1c. The thickness of flake M1 is measured to be 2.9, 2.6 and 3.1nm at three positions, which gives an average thickness as 2.86 nm(Fig.S2d). Such thickness is larger than the real monolayer(~ 0.7nm), indicating there may be a thin layer of Se adatoms existing on the top of monolayer WSe_2 flake.

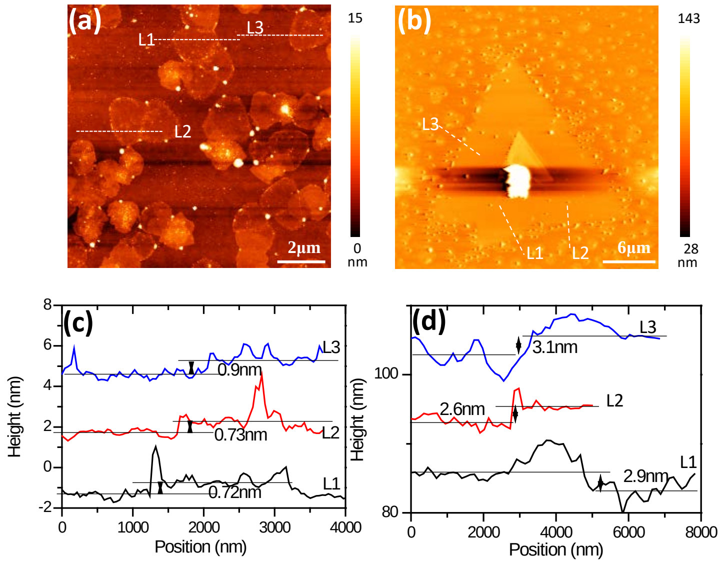

Fig. S2, (a) AFM topographic image of sample M4; (c)AFM topographic image of sample M1; (c) height line profiles recorded along marked line "L1", "L2" "L3" in Fig.S2(a). (d) height line profiles recorded along marked lines in "L1", "L2" "L3" of S2(b).

§S5 Nano Auger spectra of monolayer and few-layer WSe_2 samples.

The relative atom percentage of W and Se can be calculated from their Auger peak intensity by using the following equation(S5)[7]:

$$C_i = \frac{I_i/S_i}{\sum_{i=o}^{n} I_i/S_i} \qquad \text{(S5)}$$

Where C_i is the relative atom percentage of an element i, I_i and S_i are peak intensity and instrumental sensitive factor of this element, respectively.

The atom ratio of Se to W can also be calculated from eq.S5 as following:

$$C_{Se}/C_W = \frac{I_{Se}/S_{Se}}{I_W/S_W} \qquad \text{(S6)}$$

By using instrumental sensitive factor of Se and W as 0.038 and 0.073, respectively, the calculated atom ratio are plot in Fig.S3c.

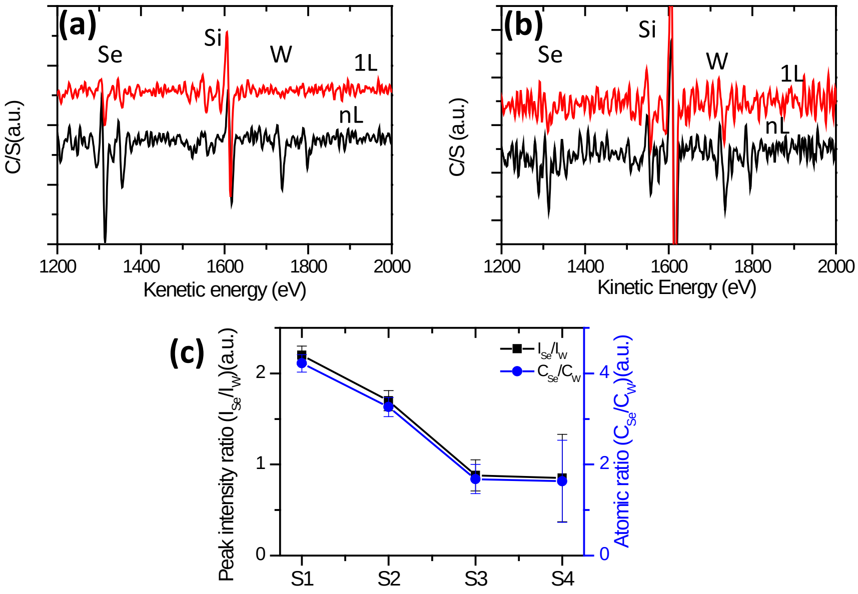

Fig.S3, Nano-Auger spectra of monolayer(1L) and thick layer(nL) in sample M1 (a) and sample M4(b). (c) Peak intensity ratio and calculated atomic ratio of Se (I_{Se})to that of W(I_W) for sample M1 to M4.

Table S1, the Auger peak intensity and calculated ratio uncertainties.

Sample	I_{Se}/ I_W	Uncertainty	C_{Se}/C_W	Uncertainty

M1	1L	3.7	3.1	7.1	6
	TL	2.3	0.4	4.3	0.8
M4	1L	0.8	0.4	1.5	0.8
	TL	0.9	0.3	1.6	0.6

By using eq.S5 and S6, the calculated atom ratio and there uncertainties are also shown in Table S1. From table S1, it can be seen that in sample M4, monolayer area gives an Se/W atom ratio as 1.5, while thick layers gives a Se/W atom ratio as 1.6. From thick layer to monolayer, the stoichiometry only change by <30%, which indicates the stoichiometry observed on thick layers is still useful to monitor the atom composition in monolayer. This method greatly reduces the stoichiometry uncertainties of monolayer sample induced by low signal to noise ratio. In M1, the stoichiometry of C_{Se}/C_W is calculated to be 7.1, with great uncertainty of 6. However, the thick layer sample only show an uncertainty of 0.75 in respect to C_{Se}/C_W as 4.3.It can be seen from table S1 that the uncertainty between thick layer and monolayer is much smaller than the uncertainties induced by the noise level. Therefore, the atom ratio calculated using Auger spectrum of thick layer samples are useful to investigate the atom ratio change in monolayer samples.

§S6 Assignment of Raman peaks of monolayer WSe_2

Table S2 Tentative assignment of Raman peaks of sample M1-M4.

Possible modes[8]	M1	M2	M3	M4
LA(M)	148	136	136	145
TA(M)+ZA(M)	220	228	226	226
E'(M)^{LO2}	244	243		242
E'(Γ)+A'(Γ)	251	251	250 255	249
A''(M)+2LA(M)	260	262	259	259

The observed Raman shift of M1-M4 are actually the emergence of different Raman modes of WSe_2. Resonant Raman measurements were performed on another Raman spectrometer using 532nm and 633 nm lasers. As shown by Fig.S4, at excitation wavelength of 633nm, four Raman modes(~222cm^{-1}, ~241cm^{-1}, ~250cm^{-1} and 259cm^{-1}) can be observed. However, which mode become prominent strongly depends on resonant Raman effect. The shift of these Raman modes in respect to their reported values[9] can also be related with the material properties. These factors can be interpreted as following:

1) Resonant Raman effect.

As shown by Fig.S4, the prominent peak observed on Raman spectrum excited by 633nm laser becomes very weak when the sample is excited by 532nm laser, while another mode at 250cm^{-1} becomes to be prominent. Such wide range Raman peak shift can be interpreted by resonant Raman effect.

According to the resonant equation in ref.[9]

$$I(E_{laser}) = C\left|\sum_{a,b}\frac{\langle f|H_{e-r}|b\rangle\langle b|H_{e-ph}|a\rangle\langle a|H_{e-r}|i\rangle}{(E_{laser}-E_g+i_\gamma)(E_{laser}-E_g+E_{ph}+i_\gamma)}\right|^2 \qquad \text{(S7)}$$

where E_{laser} is the laser photon energy , E_{ph} is the phonon energy of a Raman mode, E_g is the band gap, γ is the damping factor. The two terms in denominator give rise to the enhancement of a first-order Raman mode when the incident or scattered photon energy meet the resonant energy of an electronic or excitonic transition. Three terms in numerator correspond to the Hamiltonians of electron-photon (emission of a scattered photon) , electron-phonon (creation of a phonon), and electron-photon (absorption of an incident photon), respectively.

Since the second-order Raman process is a two-phonon process, the resonance of second-order Raman modes list in table S2 can also be partially depicted by eq.S7. The resonance of second-order Raman modes had not been well established in previous literatures. However, the resonance curves published by Corro et al[10] is still useful to interpret the observed Raman peak shift in our study.

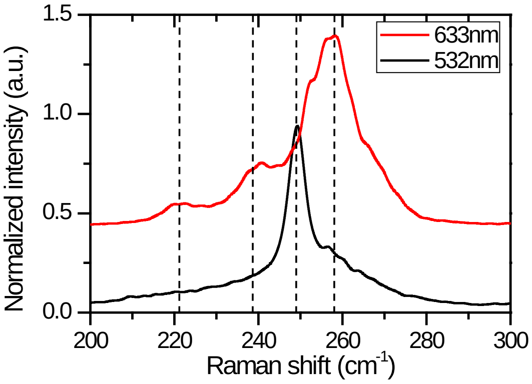

Fig.S4, Raman spectra of WSe_2 sample (M3)excited by 532nm laser and 633nm laser.

For a material with a fixed E_g, the intensity of a first-order Raman mode of WSe_2 is maximized when the denominator of eq.R1 goes to zero. This corresponds to the mode of $250cm^{-1}$ [10], whose intensity goes to maximum when the incident laser energy fits the resonance of A^- or B^- excitons. The second-order Raman mode at $260cm^{-1}$ also follows this rule.

In our study, due to instrumental limitations, E_{laser} in eq.S7 is selected at 532nm and 633nm, whereas the band gap of different samples are chaning from M1 to M4. In this case, the resonance of different Raman modes can also be observed because the second bracket of the denominator in eq.S7 also goes to zero when E_g-E_{ph} equals the laser energy E_{laser}.

Raman spectra of M1-M4 measured by 532nm and 633nm are shown in Fig.S5. It can be seen that the prominent peaks shift depends on both samples and excitation wavelength. With excitation of 532nm, the prominent peak shift 240(M1) → 249(M2) →254(M3) →259(M4)cm^{-1}. However, in spectra measured by 633nm lasers, the prominent peaks are 242(M1) →257(M2)

→275(M3) →297(M4)cm^{-1}. These wide energy shift of Raman modes of WSe_2 can be well interpreted by resonance of different modes. Such sequent blueshift from low energy mode E'(M)^{LO2} to high energy mode A''(M)+2LA(M) indicates increasing band gaps from M1 to M4[10]. It will be seen such increasing band gap agrees well with DFT calculations.

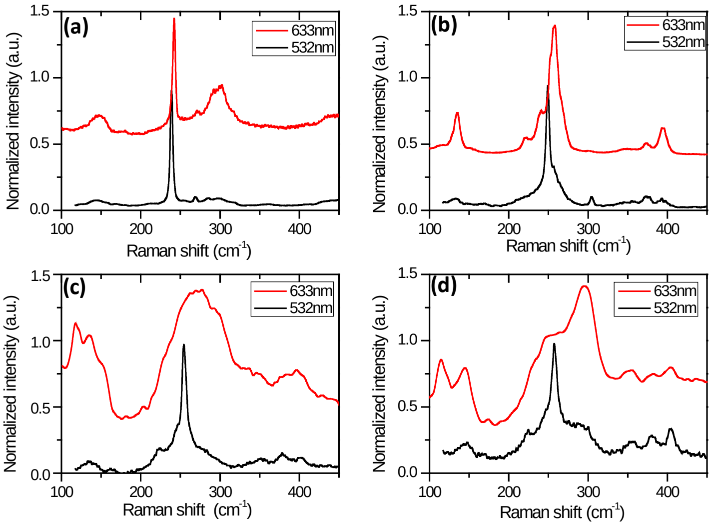

Fig.S5, Raman spectra of sample M1(a), M2(b), M3(c) and M4(d)measured by 532nm and 633nm laser.

2) Material properties fluctuation

In this study, the Raman peak positions of monolayer WSe_2 samples are also dependent on their intrinsic properties, such as strain or atomic stoichiometry, or both. Four Raman spectra are recorded from four monolayer flakes on sample M4 and shown in Fig.S6. It can be seen their Raman peak positions vary from 258.3 to 256.3cm^{-1}, which could be affected by both the strain and composition.

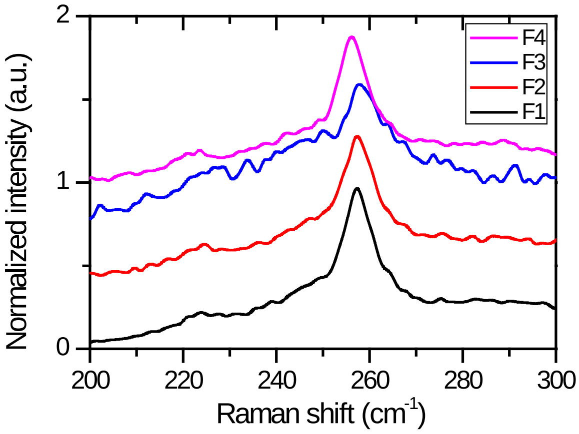

Fig. S6 Four measured Raman spectra of monolayer flakes on sample M4.

§S7 PL image of four monolayer WSe$_2$ samples.

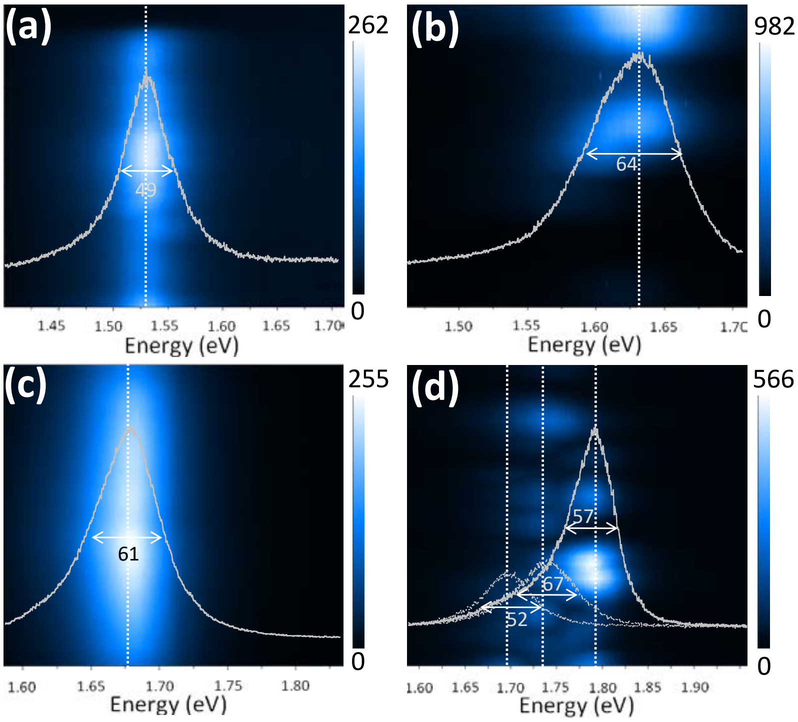

Fig.S7 Stacked PL spectra of different positions on different 1L WSe$_2$ samples: (a) M1, (b) M2, (c)M3, (d)M4; Typical PL spectrum of every sample is plotted as inset in corresponding image.

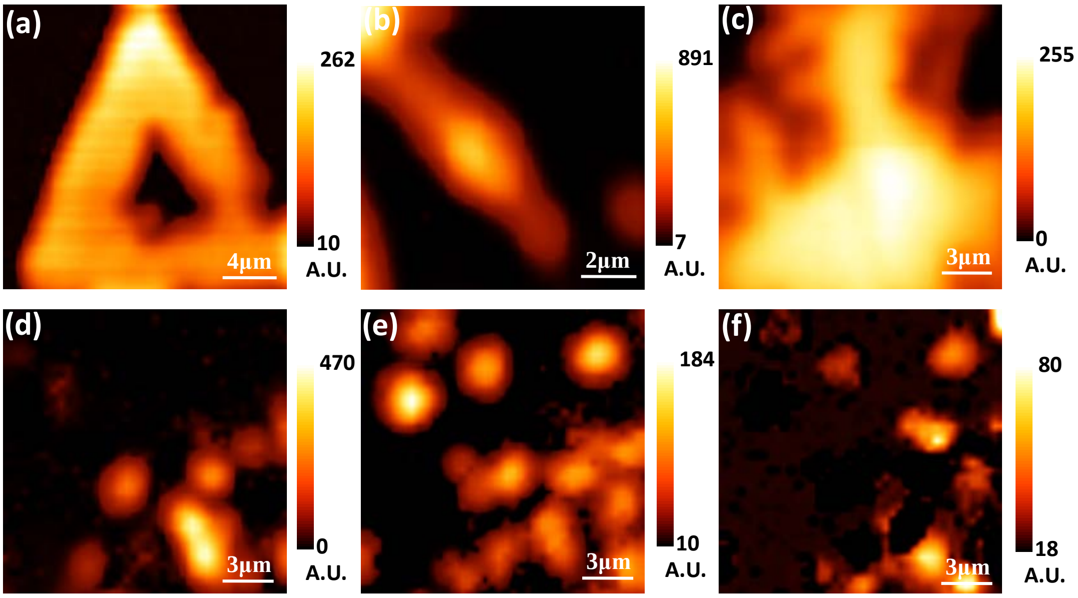

Fig.S8 PL intensity image of M1(a), M2(b), M3(c); PL intensity images of sample M4 using PL band at 1.79(d), 1.75(e), 1.72eV(f).

§S8 Lifetime measurement

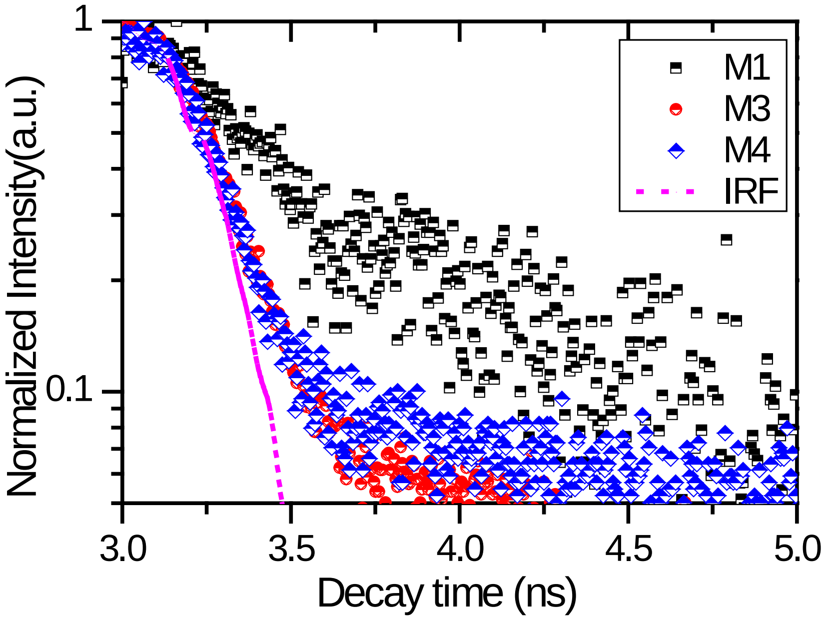

Fig. S9, PL decay curves of monolayer Sample M1, M3 and M4.

§S9 Band structures and formation energies of WSe_2 with defects

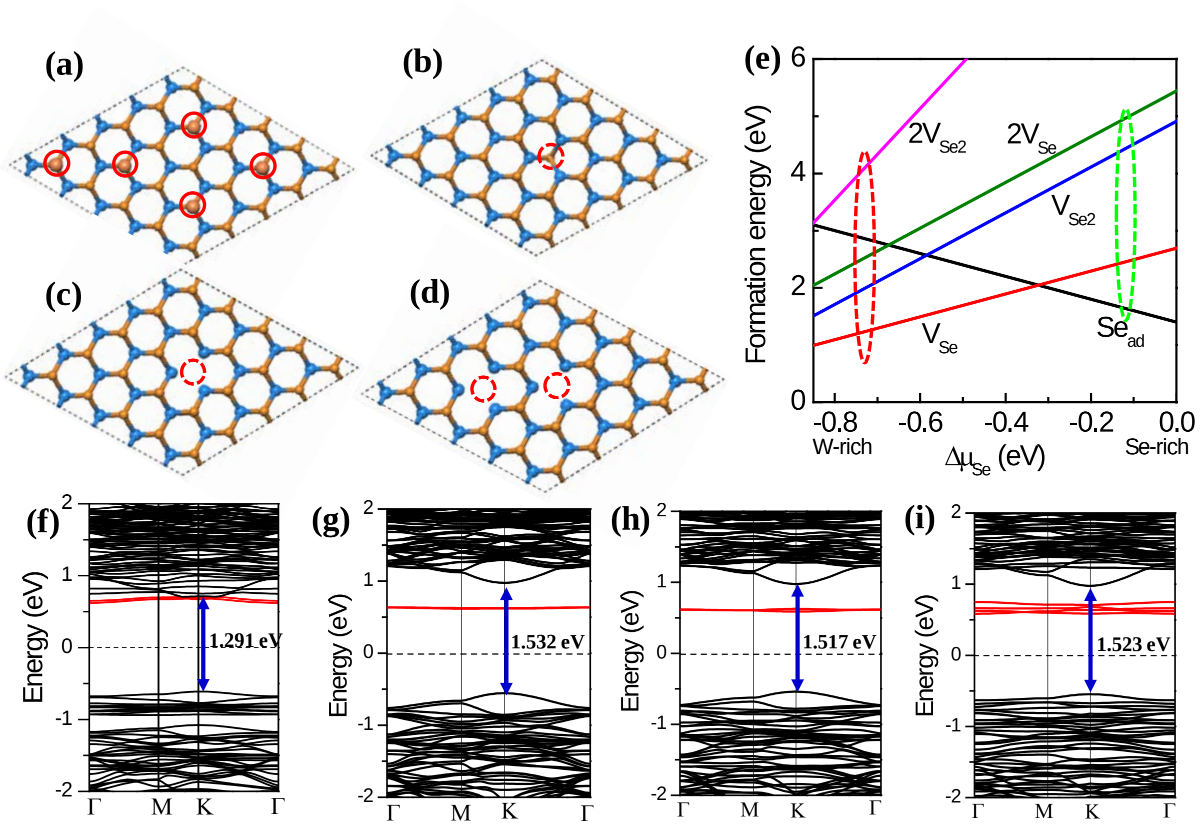

Fig. S10. Atomic structures of WSe_2 monolayer with various of Se-vacancy defects, including of (a) five Se adatoms; (b) a Se vacancy (V_{Se}), (c) a Se di-vacancy (V_{Se2}) and (d) two Se di-vacancy ($2V_{Se2}$), here Se adatoms, V_{Se}

and V_{Se2} are labeled by red circles; (e) Formation energy of various defective structures as a function of Se chemical potential $\Delta\mu_{Se}$; (f)-(i) Band structures of WSe_2 monolayer corresponding to (a)-(d), the horizontal dash lines denote the position of Fermi level and red lines represent the defect states induced by various of defects.

§S10 The influence of dielectric constants on the excitonic PL energy.

The excitonic PL energy can be calculated by $E_{exc}=E_g-E_b$, where E_g and E_b are the band gap and exciton binding energy, respectively. E_b can be calculated by the equation[11]:

$$E_b = -\frac{E_H}{\varepsilon_r^2}\left(\frac{m_r^*}{m}\right) \qquad \text{(S8)}$$

Where ε_r is the relative dielectric constant, E_H=13.6eV is the ionized energy of ground state of hydrogen atom, m_r is the effective reduced mass of electrons and holes, m is the mass of an electron.

The relative dielectric constant of WSe_2 with perfect and defective lattice are also calculated and shown in Table S3. Note that the ε_r of WSe_2 is anisotropic in plane and out of plane.

Table S3, The calculated dielectric constant and excitonic binding energy variation ratio of monolayer WSe_2

Samples	$\varepsilon_{r//}$	$\varepsilon_{r\perp}$	$\varepsilon_{r//}$ **ratio**	E_b **decreased ratio**
Perfect lattice	*7.10*	*1.59*	/	/

V_{Se}	7.24	1.59	1.97%	3.8%
$2V_{Se}$	7.41	1.59	4.37%	8%
V_{Se2}	7.30	1.58	2.81%	5%
$2V_{Se2}$	7.54	1.57	6.19%	11.1%
Se_{adatom}	7.18	1.64	1.12%	2.2%

A typical excitonic binding energy of perfect monolayer WSe_2 is assumed as 0.4eV. The adatom causes a decrease of exciton binding energy as 0.008eV, which is much smaller than the band gap decrease(0.054eV). Therefore excitonic PL energy decreasing of Se-adatom samples is dominated by the band gap decrease. As the calculated band gap of lattice with a Se adatom is 0.054eV smaller than the band gap of perfect lattice, small decrease of exciton binding energy as 0.008eV finally still induces a reduced excitonic PL energy. $2V_{Se}$ causes a decrease of exciton binding energy as 0.032eV. Combined with band gap increase as 0.01eV, finally an enlargement of excitonic PL energy is induced, which still agrees well with the increasing excitonic PL energies in Se-deficient samples.

References

1. M. Binnewies, R. Glaum, M. Schmidt and P. Schmidt, *Chemical Vapor Transport Reactions*, Walter de Gruyter GmbH & Co. KG,, Berlin/Boston, 2012.
2. G. Kresse and D. Joubert, *Physical Review B*, 1999, **59**, 1758-1775.
3. P. E. Blöchl, *Physical Review B*, 1994, **50**, 17953-17979.
4. G. Kresse and J. Furthmüller, *Physical Review B*, 1996, **54**, 11169-11186.
5. M. C. Payne, M. P. Teter, D. C. Allan, T. A. Arias and J. D. Joannopoulos, *Reviews of Modern Physics*, 1992, **64**, 1045-1097.
6. H. Sahin, S. Tongay, S. Horzum, W. Fan, J. Zhou, J. Li, J. Wu and F. M. Peeters, *Physical Review B*, 2013, **87**.
7. X. Huang and T. Xie, *Materials Analysis Techniques*, National Defence Technique Press, 2008.
8. P. Zhao, D. Kiriya, A. Azcatl, C. Zhang, M. Tosun, Y.-S. Liu, M. Hettick, J. S. Kang, S. McDonnell, K. C. Santosh, J. Guo, K. Cho, R. M. Wallace and A. Javey, *Acs Nano*, 2014, **8**, 10808-10814.
9. A. Arora, M. Koperski, K. Nogajewski, J. Marcus, C. Faugeras and M. Potemski, *Nanoscale*, 2015, **7**, 10421-10429.
10. E. del Corro, H. Terrones, A. Elias, C. Fantini, S. Feng, N. Minh An, T. E. Mallouk, M. Terrones and M. A. Pimenta, *Acs Nano*, 2014, **8**, 9629-9635.
11. X. Shen, *Semiconductor spectroscopy and optical properties*, Science Press, China, Beijing, 2002.